

See discussions, stats, and author profiles for this publication at: <https://www.researchgate.net/publication/221765514>

Structure of Mandelate Racemase with Bound Intermediate Analogues Benzohydroxamate and Cupferron

ARTICLE · FEBRUARY 2012

DOI: 10.1021/bi2018514 · Source: PubMed

CITATIONS

7

6 AUTHORS, INCLUDING:



Mitesh Nagar

University of Massachusetts Medical School

6 PUBLICATIONS 16 CITATIONS

SEE PROFILE



Elise Pellmann

Concordia University Wisconsin

1 PUBLICATION 7 CITATIONS

SEE PROFILE



Stephen Bearne

Dalhousie University

67 PUBLICATIONS 719 CITATIONS

SEE PROFILE

Published in final edited form as:

Biochemistry. 2012 February 14; 51(6): 1160–1170. doi:10.1021/bi2018514.

Structure of Mandelate Racemase with Bound Intermediate Analogues Benzohydroxamate and Cupferron†

Adam D. Lietzan[§], Mitesh Nagar[‡], Elise A. Pellmann[§], Jennifer R. Bourque[‡], Stephen L. Bearne^{‡, #}, and Martin St Maurice^{§, *}

[§]Department of Biological Sciences, Marquette University, Milwaukee, WI 53201-1881, USA

[‡]Department of Biochemistry and Molecular Biology, Dalhousie University, Halifax, NS, B3H 4R2, Canada

[#]Department of Chemistry, Dalhousie University, Halifax, NS, B3H 4R2, Canada

Abstract

Mandelate racemase (MR, EC 5.1.2.2) from *Pseudomonas putida* catalyzes the Mg²⁺-dependent interconversion of the enantiomers of mandelate, stabilizing the altered substrate in the transition state by 26 kcal/mol relative to the substrate in the ground state. To understand the origins of this binding discrimination, we solved the X-ray crystal structures of wild-type MR complexed with two analogues of the putative *aci*-carboxylate intermediate, benzohydroxamate and cupferron, to 2.2-Å resolution. Benzohydroxamate is shown to be a reasonable mimic of the transition state/intermediate since its binding affinity to 21 MR variants correlates well with changes in the free energy of transition state stabilization afforded by these variants. Both benzohydroxamate and cupferron chelate the active site divalent metal ion and are bound in a conformation with the phenyl ring coplanar with the hydroxamate and diazeniumdiolate moieties, respectively. Structural overlays of MR complexed with benzohydroxamate, cupferron, and the ground state analogue (*S*)-atrolactate reveal that the *para*-carbon of the substrate phenyl ring moves by 0.8–1.2 Å between the ground state and intermediate state, consistent with the proposal that the phenyl ring moves during MR catalysis while the polar groups remain relatively fixed. Although the overall protein structure of MR with bound intermediate analogues is very similar to MR with bound (*S*)-atrolactate, the intermediate-Mg²⁺ distance shortens, suggesting a tighter complex with the catalytic Mg²⁺. In addition, Tyr 54 moves nearer to the phenyl ring of the bound intermediate analogues, contributing to an overall constriction of the active site cavity. However, site-directed mutagenesis experiments revealed that the role of Tyr 54 in MR catalysis is relatively minor, suggesting that alterations in enzyme structure that contribute to discrimination between the altered substrate in the transition state and the ground state by this proficient enzyme are extremely subtle.

Mandelate racemase (MR, EC 5.1.2.2) from *Pseudomonas putida* catalyzes the Mg²⁺-dependent 1,1-proton transfer that interconverts the enantiomers of mandelate via a two-base

[†]This work was supported by the National Institute of Health grant GM070455 (M. St. M.) and a Discovery Grant from the Natural Sciences and Engineering Research Council (NSERC) of Canada (S.L.B.). ADL is supported by a GAANN award (Graduate Assistance in Areas of National Need) from the U.S. Department of Education.

* Author to whom correspondence should be addressed. Phone: (414) 288-2087; fax: (414) 288-7357; martin.stmaurice@marquette.edu.

Accession codes. The atomic coordinates for MR+BzH and MR+CfN have been deposited in the Protein Data Bank as entry 3UXK and 3UXL, respectively.

Supporting information. Supplementary Table S1 and supplementary Figures S1 and S2 are provided in the supporting information. This material may be accessed free of charge online at <http://pubs.acs.org>.

mechanism with His 297 and Lys 166 abstracting the α -proton from (*R*)-mandelate and (*S*)-mandelate, respectively, as shown in Figure 1 (1). MR is very proficient at discriminating between the substrate in the ground state and the altered substrate in the transition state (TS), binding the latter species with an association constant equal to $5 \times 10^{18} \text{ M}^{-1}$ and stabilizing the TS of the reaction by 26 kcal/mol (2, 3). Consequently, the enzyme has been studied as a paradigm for understanding enzyme-catalyzed proton abstraction from carbon acids (1, 4–7). Enzymes such as MR, that are extremely proficient at stabilizing the TSs and intermediates formed during catalysis, are often strongly inhibited by analogues of either the altered substrate in the TS or unstable intermediates that resemble the TS (8–12). Our interest in understanding how binding determinants within the active site of MR stabilize the TS for α -proton abstraction led us to survey a series of reactive intermediate analogues as potential TS or intermediate analogue inhibitors (13–16), leading to the identification of α -hydroxybenzylphosphonate ($K_i = 4.7 \text{ }\mu\text{M}$, (15)), benzohydroxamate (BzH, $K_i = 9.3 \text{ }\mu\text{M}$, (15)), *N*-hydroxyformanilide ($K_i = 2.8 \text{ }\mu\text{M}$, (13)), and cupferron (CfN, $K_i = 2.7 \text{ }\mu\text{M}$, (13)) as potent reversible competitive inhibitors of MR. As shown in Figure 1, both BzH and CfN may be regarded as analogues of the *aci*-carboxylate intermediate.

Herein, we report a critical analysis of TS mimicry by BzH along with the first structures of MR complexed with the intermediate analogues BzH and CfN. The primary determinant of high affinity binding in MR originates from the coordination of Mg^{2+} in the active site. The hydrophobic pocket surrounding the aromatic ring constricts around the intermediate analogues, consistent with the contribution of this region to transition state stabilization. In general, however, there appear to be few specific enhanced contacts with analogues of the *aci*-carboxylate intermediate.

MATERIALS AND METHODS

General

(*R*)- and (*S*)-Mandelic acid, benzohydroxamate, and all other reagents, unless mentioned otherwise, were purchased from Sigma-Aldrich Canada Ltd. (Oakville, ON, Canada). Cupferron (NH_4^+ -salt) was purchased from Fisher Scientific (Ottawa, ON, Canada). Circular dichroism (CD) assays and spectral measurements were conducted using a JASCO J-810 spectropolarimeter.

Enzyme purification

For X-ray crystallography studies, recombinant MR from *Pseudomonas putida* was overproduced in and purified from *Escherichia coli* BL21(DE3) cells transformed with the pET-52b(+)-WTMR plasmid, a pET-52b(+) plasmid (Novagen, Madison, WI) containing the MR open reading frame (ORF) (17). This construct encodes the MR gene product (MASWSHPQFEKGALEVLFGQPGYHM₁...MR) with an N-terminal StrepII-tag (underlined; M₁ represents the first amino acid of wild-type MR). The enzyme was purified by affinity chromatography using *Strep*-Tactin Superflow resin (IBA GmbH, Göttingen, Germany) as described previously (17). Upon elution from the column, the enzyme was dialyzed against storage buffer (HEPES buffer (100 mM, pH 7.5) containing MgCl_2 (3.3 mM), NaCl (200 mM), and glycerol (10% v/v)) and stored at -20°C . Four-five enzyme preparations were then pooled, dialyzed against HEPES buffer (50 mM, pH 7.5) containing MgCl_2 (3.3 mM) and NaCl (50 mM), and concentrated to $\sim 10 \text{ mg/mL}$ using an Amicon Ultracel-10K centrifugal filter unit (Fisher Scientific, Ottawa, ON). The tag was not removed from the enzyme and the enzyme preparation was immediately frozen as 50 μL aliquots in thin-walled, 250- μL polypropylene microcentrifuge tubes in liquid nitrogen and stored at -80°C .

Site-directed mutagenesis

With the exception of the Y54F and Y54L variants, mutant mandelate racemases bearing an N-terminal hexahistidine tag were prepared and purified as described previously (15, 18–20). For the Y54F and Y54L MRs, the pET-52b(+)-WTMR plasmid was used as the template for polymerase chain reaction-based site-directed mutagenesis using the QuikChange Site-Directed Mutagenesis Kit (Stratagene, La Jolla, CA) and following the protocols described by the manufacturer. The forward (F) and reverse (R) synthetic deoxyoligonucleotide primers used to incorporate the desired mutation in the ORFs encoding the Y54F and Y54L MRs are listed in Table S1. After site-directed mutagenesis, mutant plasmids were used to transform competent *E. coli* DH5α cells for plasmid maintenance. Each mutant ORF was sequenced using commercial automated sequencing (Robarts Research Institute, London, ON) to ensure that no other alterations in the nucleotide sequence had been introduced. *E. coli* BL21(DE3) cells were used as the host for target gene expression and the overproduced StrepII-tagged mutant MRs were purified as described previously (17).

Enzyme assays

MR activity was assayed using a CD-based assay by following the change in ellipticity of mandelate at 262 nm with a 1 cm light path (unless otherwise indicated) as described by Sharp *et al.* (21). All assays were conducted at 25 °C in Na⁺-HEPES buffer (0.1 M, pH 7.5) containing MgCl₂ (3.3 mM, unless mentioned otherwise) and bovine serum albumin (BSA, 0.005%). The concentrations of (*R*)- and (*S*)-mandelate for assays of all mutant MR enzymes ranged between 0.25 and 10.0 mM.

Competitive inhibition experiments with BzH were conducted in Na⁺-HEPES buffer (0.1 M, pH 7.5) containing MgCl₂ (3.3 mM, unless mentioned otherwise) and (*R*)-mandelate (0.5–20.0 mM). Enzyme concentrations and assay details have been described previously (15, 18–20). For the inhibition experiments, the concentrations of the mutant enzyme and BzH used, respectively, were: wild-type (150 ng/mL; 20, 40, & 60 μM), Y54F (158 ng/mL; 10, 20, 30, & 40 μM), Y54L (321 ng/mL; 25, 50, & 75 μM; using a cuvette with a 0.5 cm light-path), V22A (300 ng/mL; 200, 400, & 600 μM), V22I (150 ng/mL; 20, 40, & 60 μM), V22F (300 ng/mL; 100, 200, & 400 μM), T24S (450 ng/mL; 100, 200, & 300 μM), A25V (500 ng/mL; 200, 400, & 600 μM), V26A (150 ng/mL; 25, 50, & 75 μM), V26L (450 ng/mL; 200, 400, & 600 μM), V26F (450 ng/mL; 300, 500, & 700 μM), V26A/V29L (500 ng/mL; 50, 100, & 200 μM), V29A (150 ng/mL; 150, 300, & 600 μM), V29L (150 ng/mL; 20, 40, & 80 μM), and V29F (450 ng/mL; 60, 90, & 120 μM). Inhibition constants (*K_i*) were determined by fitting the initial velocity data to eqn. 1 using nonlinear regression analysis and the program *KaleidaGraph* v. 4.02 from Synergy Software (Reading, PA). All kinetic parameters were determined in triplicate and average values are reported. The reported errors are standard deviations. The concentrations of variant MRs were determined using either the Bio-Rad protein assay (Bio-Rad Laboratories, Mississauga, ON, Canada) with BSA standards, or from their absorbance at 280 nm using extinction coefficients of 53 400 M⁻¹ cm⁻¹ (wild-type) or 51 910 M⁻¹ cm⁻¹ (Y54F and Y54L) that were calculated using the ProtParam tool available on the ExPASy server (<http://web.expasy.org/protparam>) (22).

$$v_i = \frac{V_{\max}[S]}{K_m(1 + [I]/K_i) + [S]} \quad (1)$$

Protein Crystallization

Crystals for the BzH and CfN complexes with MR were grown by the hanging-drop vapor diffusion method against a 500 μ L reservoir volume. The protein solution and reservoir solution were mixed in a 1:1 ratio to a final volume of 4 μ L. Crystals grew spontaneously at 21 °C and ~50% humidity.

MR with BzH—For the MR crystals grown in the presence of BzH, the reservoir solution consisted of PEG 1500 (14%), glycine (200 mM), NaI (50 mM), and triethanolamine (100 mM, pH 8.0). The protein solution consisted of 6.4 mg/mL MR purified as described above, $MgCl_2$ (3.3 mM), BzH (2 mM), and HEPES buffer (50 mM, pH 7.5). The resulting cube-like crystals (~65 μ m \times 65 μ m \times 40 μ m) grew to full size within 5–10 days. After 15 days, the crystals were harvested and transferred to a synthetic stabilizing solution consisting of PEG 1500 (24%), glycine (210 mM), NaI (50 mM), BzH (2 mM), and triethanolamine buffer (80 mM, pH 8.0). These stabilized crystals were transferred in 4 successive steps to a cryoprotectant solution at ratios of 3:1, 1:1, 1:3, and 0:4 (synthetic:cryoprotectant), with an equilibration time of 5–10 min between transfers. The cryoprotectant consisted of PEG 1500 (38%), glycine (210 mM), NaI (50 mM), BzH (3 mM), and triethanolamine buffer (80 mM, pH 8.0). The cryoprotected crystals were flash-cooled in a nitrogen gas stream at 100 K.

MR with CfN—For the MR crystals grown in the presence of CfN, the reservoir solution consisted of PEG 1500 (20%), glycine (120 mM), NaI (50 mM), and Bis-tris propane buffer (100 mM, pH 9.3). The protein solution consisted of 6.4 mg/mL MR purified as described above, $MgCl_2$ (3.3 mM), CfN (2 mM), and HEPES buffer (50 mM, pH 7.5). The resulting cube-like crystals (~65 μ m \times 65 μ m \times 40 μ m) grew to full size within 5–10 days. After 38 days, the crystals were harvested and transferred directly to a cryoprotectant solution consisting of PEG 1500 (44%), glycine (150 mM), CfN (2 mM), and Bis-tris propane (100 mM, pH 9.3), with an equilibration time of 5–10 min. The cryoprotected crystals were flash-cooled in a nitrogen gas stream at 100 K.

Data collection, structure determination, and refinement

X-Ray diffraction data were collected at the Advanced Photon Source (APS) beamline LS-CAT-21-ID-F on a Rayonix MarMosaic 225 CCD detector, with an X-ray wavelength of 0.978 Å. Diffraction images were processed using HKL2000 (23). The structures were solved by molecular replacement using the wild-type MR enzyme (pdb 2MNR) as the search model with the program Phaser (24). The molecular replacement models were extended by several rounds of manual model building with COOT (25) and refinement with REFMAC (26) using a geometric/X-ray weighting term of 0.2. Non-crystallographic restraints between each monomer were applied for the first round of refinement, but were relieved for subsequent rounds. Water molecules were added to the model in COOT with subsequent manual verification. CfN ligand coordinates were generated and optimized for structure refinement using electronic ligand building and optimization workbench (eLBOW) (27). Data collection and processing statistics are summarized in Table 1.

RESULTS AND DISCUSSION

Transition state mimicry

Hydroxamates have been used as structural mimics of *aci*-carboxylate intermediates in the characterization of several enolase superfamily enzymes (28–31). BzH is a structural and electronic mimic of the *aci*-carboxylate intermediate and is bound by MR with an affinity that is 100-fold greater than that exhibited for the substrate (15). The high binding affinity of BzH, however, is not sufficient evidence to classify BzH as a transition state analogue. The degree to which an intermediate/TS analogue mimics the structural and electronic character

of the true TS can be assessed by comparing the effects of equivalent structural perturbations on the binding affinity of the altered substrate in the TS (via effects on $k_{\text{cat}}/K_{\text{m}}$) and on the binding affinity of the putative TS analogue (via effects on K_{i}) (32, 33). Based on eqn. 2, where k_{non} is the first order rate constant for reaction in the absence of enzyme and K_{tx} is the virtual dissociation constant for the enzyme-substrate complex in the TS, a correlation between the free energy accompanying inhibitor binding (from $1/K_{\text{i}}$ values) and the relative free energies of activation (from $k_{\text{cat}}/K_{\text{m}}$ values) for a variety of mutant enzymes catalyzing the same reaction is expected (32, 33). If a TS analogue inhibitor captures a significant portion of the binding free energy expected for the altered substrate in the TS, then the observed binding affinity, K_{i} , should approximate K_{tx} . Table 2 shows the values of K_{m} , k_{cat} , and $k_{\text{cat}}/K_{\text{m}}$ for wild-type MR and 20 variants along with the competitive inhibition constants for inhibition of these enzymes by BzH. The linear free energy relationship relating the relative free energies of activation for the wild-type and variant enzymes to the corresponding free energies of BzH binding is shown in Figure 2A. While the slope is unity, the correlation is weak ($r^2 = 0.74$). However, the linear free energy relationship relating the relative free energies of substrate binding (from $1/K_{\text{m}}$ values) to free energies of inhibitor binding (Figure 2B) has a slope of only 0.25 and a much weaker correlation ($r^2 = 0.14$), showing that BzH does indeed exhibit mimicry of the altered substrate in the TS and is not simply acting as a ground state analogue. A detailed analysis of the linear free energy relationship has not been performed for CfN. However, it is isosteric and isoelectronic with BzH (Figure 1) and is bound by the enzyme with high affinity (13). On this basis, and given that it is bound by MR in a manner analogous to BzH (*vide infra*), CfN may also be regarded as a mimic of the *aci*-carboxylate intermediate.

$$\log\left(\frac{k_{\text{cat}}}{K_{\text{m}}}\right) = \log k_{\text{non}} + \log\left(\frac{1}{K_{\text{tx}}}\right) \quad (2)$$

BzH possesses two sites of deprotonation (i.e., oxygen and nitrogen); therefore, several structures may exist in solution. This is also the case for CfN. In water, BzH exists primarily in the keto form and experimental evidence suggests that BzH undergoes *O*-deprotonation in water (34), yielding a species that does not closely resemble the putative *aci*-carboxylate intermediate. The pH-dependence of BzH inhibition of MR is consistent with the deprotonated form of BzH being preferentially bound by the enzyme (15). The *O*-deprotonated enol form of BzH has never been observed in water; however, this form of BzH (*cis* or *trans*) more closely resembles the structure of the putative *aci*-carboxylate intermediate and may therefore be preferentially stabilized within the active site of MR (15).

While BzH and CfN embody certain features of the high-energy intermediate, they are not perfect analogues of the transition state for several reasons. First, the electrostatic potential surfaces of BzH and CfN do not perfectly mimic the putative intermediate (Figure 1). Second, BzH and CfN lack an oxygen that is present in the *aci*-carboxylate intermediate, which does impose a limitation on the present structural analysis. Gerlt and Gassman (6) have suggested that the most effective transition state analogue inhibitors for MR will have $\text{p}K_{\text{a}}$ values that match that of the intermediate. According to Gerlt and Gassman, the $\text{p}K_{\text{a}}$ of the neutral intermediate is critical to the formation of a short, strong H-bond between the general acid catalyst Glu 317 and the intermediate, which stabilizes the intermediate thereby lowering its energy. If, indeed, formation of a short, strong H-bond with Glu 317 dominates the stabilization of the intermediate, then this may limit the extent of mimicry afforded by BzH and CfN. In the current structures, the intermediate analogues do not interact with Glu 317 because the hydroxamate and diazeniumdiolate groups of BzH and CfN, respectively, assume a *cis* geometry and chelate the Mg^{2+} within the enzyme's active site (*vide infra*). Even if BzH and CfN were bound with the *trans* geometry permitting interaction with Glu

317, their respective pK_a values of 8.8 (34, 35) and 4.2 (36–38) are several units removed from the pK_a of Glu 317 (estimated to be ~6 in MR (6, 39)). Although the inability of BzH to interact with Glu 317 may attenuate the degree to which BzH serves as a perfect mimic of the *aci*-carboxylate intermediate/TS, the linear free energy relationship and structural features of BzH indicate that BzH does respond to changes in transition state stabilization afforded by MR variants.

General description of MR structure

MR is composed of three distinct structural domains (40): an N-terminal capping domain made up of a three-stranded β -sheet with an antiparallel four α -helix bundle, a central domain consisting of a $(\beta/\alpha)_7$ β -barrel, and a short C-terminal domain composed of external β -strands. As with all TIM-barrel enzymes, the active site is located at the C-terminal ends of the β -strands near the mouth of the barrel. The majority of residues involved in ligand binding, metal ion coordination, and catalysis extend from the β -strands of the barrel (41–43). Residues located in the N-terminal capping domain form a hydrophobic cavity that contributes to substrate specificity. This cavity may be partitioned into an *R*-specific and *S*-specific pocket (Figure 3) where the phenyl group of (*R*)- and (*S*)-mandelate, respectively, is bound upon entering the active site (19, 20). Existing X-ray crystal structures include inorganic sulfate (40), (*S*)-mandelate (41), or the substrate analogue (*S*)-atrolactate (42–44) bound in the active site but there is no structural information available regarding the binding orientation of the planar *aci*-carboxylate intermediate in the active site.

The X-ray crystal structures of MR complexed with the intermediate analogues, BzH and CfN, were each determined to 2.2-Å resolution. In both structures, MR is a homo-octamer generated from a tetramer of dimers. Each dimer pair is generated through a tight association between neighboring subunits, with both members of the pair contributing residues to the neighboring active site (40). Unlike previously reported MR crystal structures, both of the current structures were determined from crystals in the space group I4 and included two separate dimers in the asymmetric unit. Each dimer forms an independent octamer through crystallographic symmetry (Figure S1). The two dimers are nearly identical; the only differences between them are two slight twists in the first and second helices of the $(\beta/\alpha)_7$ β -barrel (Figure S2). This small difference between the two octamers is sufficient to render the symmetry non-crystallographic but does not influence the packing of the octamer nor the conformation in the individual active sites. Consequently, descriptions of intermediate analogue binding are limited to one representative active site, with all other active sites being identical in their interactions.

Structures of BzH and CfN in the active site

The electron density for the BzH and CfN ligands is well-defined over the entire molecule in all four active sites, though the carbon atoms in the aromatic ring of BzH have higher relative temperature factors than the rest of the molecule (Figure 4). The root mean squared deviations (RMSDs) for structural alignments of the chain A α -carbon atoms of MR bound to (*S*)-atrolactate (pdb 1MDR) with MR bound to BzH and CfN are 0.32 Å and 0.38 Å, respectively. The RMSDs for alignment of the chain A α -carbon atoms of the apo MR structure (pdb 2MNR) with the structures of MR bound to BzH and CfN are 0.32 Å and 0.36 Å, respectively. Hence, there is no crystallographic evidence for large structural changes accompanying the enzyme's transition from the unbound state to the (*S*)-bound ground state to the intermediate-bound state. There are also no gross differences in the conformation of the 20s or 50s loops between the ground-state-bound and intermediate-bound structures (Figure 5B). Indeed, comparison of the structures of MR complexed with the ground state analogue (*S*)-atrolactate with the structures of MR complexed with the intermediate analogues BzH and CfN reveals that the positions of only a few amino acid side chains are

altered. Relative to its position in the (*S*)-atrolactate-bound structure, Lys 166, the (*S*)-specific general base catalyst, moves into closer proximity of the α -carbon of the planar intermediate analogues (Figure 5A). Since MR is a pseudosymmetric enzyme (45) with k_{cat} values in the *S*→*R* and *R*→*S* reaction directions being approximately equal, one would anticipate that both Lys 166 and His 297 would be in nearly equal proximity to the α -carbon of the *aci*-carboxylate intermediate and equally poised to protonate it (Figure 1). The structure of MR with bound BzH is in agreement with this expectation and this is the first structure of liganded-MR in which the ζ - and ϵ 2-nitrogens of Lys 166 and His 297 are positioned equidistant from the α -carbon of the ligand (i.e., 3.3 Å and 3.4 Å, respectively). The general acid/base catalysts are also in nearly equal proximity to the nitrogen atom attached to the phenyl ring of CfN, with distances of 3.2 Å and 3.4 Å to the ϵ -nitrogen of Lys 166 and His 297, respectively (data not shown). The equal distance of the general acid/base catalytic residues from the α -carbon equivalent of the intermediate analogues suggests that these structures provide a genuine snapshot of the conformation of MR attained upon binding the *aci*-carboxylate intermediate during catalysis. Alternatively, the position of the Lys166 side-chain observed in the current structures may represent the *bona fide* position of the (*S*)-specific general base throughout catalysis. In previous structures of MR complexed with (*S*)-atrolactate (42–44), steric interactions between the Lys 166 side chain and the α -methyl group of (*S*)-atrolactate may have pushed the side chain of Lys 166 farther from the substrate than may truly be the case when the (*S*)-mandelate substrate is bound.

Hydrophobic effects contribute to transition state stabilization by MR (46), suggesting a possible role for hydrophobic cavity residues in specifically stabilizing the altered substrate in the TS. However, no major changes in the positions of hydrophobic amino acid side chains located in the hydrophobic cavity can be confidently identified in the structures of MR with either bound CfN or BzH at 2.2 Å-resolution. That said, Tyr 54, which is part of the 50s loop of the *S*-specific pocket (19), does appear to change its orientation slightly in the intermediate-bound state, moving closer to the phenyl ring of BzH and CfN, thereby raising the possibility that it may interact with the phenyl ring of the *aci*-carboxylate intermediate during catalysis (Figure 5B). To assess whether Tyr 54 plays a specific role in TS stabilization by MR, the Y54F and Y54L mutants were generated and the impact of these mutations on the interconversion of (*R*)- and (*S*)-mandelate was determined. Relative to wild-type MR, the Y54F mutation had negligible effects on the values of K_{m} , k_{cat} , and $k_{\text{cat}}/K_{\text{m}}$ when either (*R*)- or (*S*)-mandelate was the substrate, and the binding affinity of BzH was not altered significantly in this mutant (Table 2). Hence, interactions with the hydroxyl group of Tyr 54 do not play a significant role in TS stabilization. If the aromatic ring of Tyr 54 plays a specific role in TS stabilization, then the Y54L mutation should exhibit a much more significant effect on $k_{\text{cat}}/K_{\text{m}}$ than on K_{m} for (*R*)- and (*S*)-mandelate. Conversely, if Tyr 54 contributes generally to the packing of the hydrophobic cavity, the Y54L mutation is expected to have an effect on both substrate binding (manifested in K_{m} for (*R*)- and (*S*)-mandelate, since $K_{\text{m}} = K_{\text{S}}$ for MR (3)) and TS stabilization (manifested in $k_{\text{cat}}/K_{\text{m}}$). The Y54L mutation results in a ~2-fold increase in K_{m} over the wild-type enzyme and a 3.5-fold decrease in $k_{\text{cat}}/K_{\text{m}}$ when either (*R*)- or (*S*)-mandelate is the substrate (Table 2). Interestingly, the effect of the Y54L mutation on the steady-state kinetic parameters is much less than the effect observed upon mutation of several other hydrophobic pocket residues (Table 2). Thus, the motion of the Tyr 54 side chain is likely a consequence of altered packing rearrangements in the hydrophobic pocket rather than a result of a specific role for Tyr 54 in TS stabilization. Nevertheless, the movement of Tyr 54 combined with a modest movement of other hydrophobic cavity side-chains such as Phe 52 (Figure 5B) suggests that the entire hydrophobic cavity may contract around the planar intermediate. Indeed, estimation of the size of the hydrophobic cavity using VOIDOO (<http://xray.bmc.uu.se/usf/voidoo.html>) (47) indicates that the size of the hydrophobic cavity shrinks from approximately 39 Å³ in the MR-(*S*)-atrolactate complex (pdb 1MDR) to

approximately 29 Å³ and 25 Å³ in the MR-BzH and MR-CfN complexes, respectively (Figure 5C). Much of this reduction in cavity volume results from the movement of Lys 166; but, there is also a notable reduction in the cavity of the hydrophobic pocket. These observations account for the observed contribution of hydrophobic interactions to TS stabilization (46).

The structures of MR with BzH and CfN also suggest enhanced coordination of Mg²⁺ by the intermediate analogues relative to the ground-state analogue (*S*)-atrolactate. BzH and CfN are bound in nearly equivalent positions and conformations in the enzyme active site, though the two ligands pivot slightly about the central α -carbon, resulting in a modest deviation in the position of the aromatic ring in the hydrophobic cavity (Figure 5B). The ligand atoms responsible for chelating Mg²⁺ are also in nearly identical positions between the structures of MR with bound intermediate and ground-state analogues (Figure 6). Superposition of the structures of MR complexed with BzH, CfN, and (*S*)-atrolactate reveals that, while the enzyme residues responsible for chelating Mg²⁺ do not change in their position or orientation, the distances between the chelating oxygen atoms of these compounds and the Mg²⁺ ion do vary. The distances between the Mg²⁺ and the chelating oxygen atoms of the carboxylate and the hydroxyl groups of (*S*)-atrolactate are 2.2 Å and 2.3 Å, and the corresponding distances in the BzH and CfN complexes are 2.2 Å and 2.1 Å, and 2.0 Å and 2.1 Å, respectively. The decreased distances between the chelating oxygens of BzH and CfN and the Mg²⁺ ion suggest that a stronger interaction exists with the Mg²⁺ ion than is present in the ground state structure. Thus, some portion of the enhanced binding affinity observed for both BzH and CfN may result from their higher relative affinity for Mg²⁺ as compared to ground state ligands (35, 48). Although the enhanced binding of BzH and CfN, relative to that observed for the ground state analogue (*S*)-atrolactate ($K_i = 0.15$ mM, (42)), may arise, in part, because BzH and CfN are better chelators of the Mg²⁺ ion, we do not consider Mg²⁺-chelation to be a feature that is independent of TS mimicry. Enhanced interaction with the divalent metal ion is an expected feature of the *aci*-carboxylate intermediate, which bears an additional negative charge relative to (*R*)- or (*S*)-mandelate, or (*S*)-atrolactate. If the high affinity of BzH was primarily a result of Mg²⁺-chelation properties of the hydroxamate functional group, one would expect MR to bind acetohydroxamate ($K_i = 27$ mM) with greater affinity than is observed (46) since the stability constants for complexes of BzH and acetohydroxamate with Mg²⁺ are similar (35). Consequently, other interactions with the enzyme beyond chelation effects (e.g., hydrophobic and polar interactions (46)) must also contribute to the high binding affinity of BzH.

Substrate motion during catalysis

Analysis of site-directed mutagenesis studies (19) and competitive inhibition of MR by benzilate (46), led us to propose that the phenyl ring of mandelate traverses the hydrophobic cavity as the enzyme interconverts (*R*)- and (*S*)-mandelate. However, the magnitude of the motion remains unknown. Two scenarios have been envisioned for this phenyl motion (Figure 7A) (19). In one scenario, the β -carbon (carbon 1 of the phenyl ring) remains stationary throughout the reaction, maintaining a plane with the carboxylate and hydroxyl groups. In this scenario, the α -carbon moves by ~1.0 Å as it undergoes Walden inversion and the *para*-carbon of the phenyl ring moves by ~1.8 Å. Alternatively, in the second scenario, the α -carbon remains fixed throughout catalysis, resulting in a greater compensatory movement of the phenyl ring (~2.8 Å at the *para*-carbon) as it pivots about the α -carbon. The crystal structures of MR with BzH and CfN offer some insight into distinguishing between these two scenarios and suggest that the α -carbon moves and the position of the β -carbon remains roughly fixed. Structural overlays of MR with the bound intermediate-analogues compared with bound (*S*)-atrolactate (Figure 7B) reveal that (i) the α -carbon moves 0.7–0.8 Å from the position it occupies in (*S*)-atrolactate to the position it

occupies in the planar intermediate analogues, (ii) the β -carbon remains fixed in a nearly identical position, and (iii) the *para*-carbon of the aromatic ring moves between 0.8–1.2 Å. Consequently, the observed movement of the *para*-carbon suggests that the total distance traversed through the hydrophobic cavity by the *para*-carbon of the phenyl ring upon interconversion of (*S*)- and (*R*)-mandelate is on the order of 1.6–2.4 Å, reduced slightly from the value of 2.8 Å (Figure 7A) by the compensating movement of the α -carbon during catalysis. Of course, a smaller range of substrate motion in the hydrophobic pocket requires fewer rearrangements of the hydrophobic cavity during catalysis.

MR, like all members of the enolase superfamily MR subgroup, orients the substrate such that it coordinates the essential Mg^{2+} using one carboxylate oxygen and the α -OH group (49). In all enolase superfamily enzymes, the α -carbon transitions from sp^3 to sp^2 hybridization as the reaction progresses from the substrate to the enolate intermediate, and the resulting structural rearrangements in the substrate have, in some instances, been proposed to play a direct role in the catalytic mechanism. For example, L-rhamnonate dehydratase, a member of the MR subgroup, has a single general acid/base residue in the active site. The transition from sp^3 to sp^2 hybridization of the α -carbon in the enolate intermediate is proposed to facilitate movement of the β -carbon, permitting His 329 to function both as the general base to deprotonate the α -carbon and as the general acid to facilitate departure of the β -OH group in the *syn*-dehydration reaction (50). The structures of MR with bound intermediate analogues suggest that, for members of the MR subgroup, which orient the substrate to coordinate Mg^{2+} with the α -OH group, the β -carbon is not likely to undergo significant movement as the reaction proceeds from the ground state to the intermediate state. Rather, the general acid/base catalyst itself may move into closer proximity to the intermediate. Just such a movement is observed for Lys 166 in MR when the structure of MR with bound (*S*)-atrolactate is compared with the structures of MR with bound intermediate analogues (Figure 5A), bearing in mind the caveat outlined above concerning the steric effect of the α -CH₃ group of (*S*)-atrolactate. Structures of galactarate/L-talarate dehydratase, another member of the enolase superfamily MR subgroup, complexed both with a hydroxamate intermediate analogue and the substrate also reveal greater movement of the α -carbon than the β -carbon (31). However, it is important to note that the introduction of a mutation in the general base, K197A, makes it difficult to directly compare the relative movement of these atoms in the structures since the entire ligand shifts in the direction of the void created by the K197A mutation in the galactarate/L-talarate dehydratase structure.

Conclusions

The crystal structures of MR with the bound intermediate analogues BzH and CfN reveal several structural features that had not been evident in the previously reported structures of MR with bound ground state analogues (40–44). These are the first structures of MR bearing a ligand in which the general acid-base catalysts, Lys 166 and His 297, are located equidistant from the α -carbon of the ligand. The distance between the chelating oxygen atoms of the intermediate analogues and the Mg^{2+} shortens slightly, relative to the corresponding distances in the ground state structure, suggesting that both BzH and CfN form a tighter complex with the catalytic Mg^{2+} as would also be expected for the *aci*-carboxylate intermediate. Tyr 54 moves nearer to the phenyl ring of the bound intermediate analogues and there is a concomitant constriction of the hydrophobic cavity within the active site. Finally, the *para*-carbon of the phenyl ring of the substrate pivots about the β -carbon by 0.8–1.2 Å between the ground state and intermediate state, consistent with the proposal that the phenyl ring moves during MR catalysis while the polar groups remain relatively fixed. The overall protein architecture of the active site of MR with either BzH or CfN bound is very similar to MR with bound (*S*)-atrolactate, suggesting that the alterations in enzyme

structure contributing to discrimination between the altered substrate in the transition state and the ground state by this proficient enzyme are extremely subtle.

Supplementary Material

Refer to Web version on PubMed Central for supplementary material.

ABBREVIATIONS

BSA	bovine serum albumin
BzH	benzohydroxamate
CD	circular dichroism
CfN	cupferron
HEPES	4-(2-hydroxyethyl)piperazine-1-ethanesulfonic acid
MR	mandelate racemase
ORF	open reading frame
TS	transition state
VDW	van der Waals

References

- Gerlt, JA. Enzyme-catalyzed proton transfer reactions to and from carbon. In: Hecht, SM., editor. *Bioorganic Chemistry: Peptides and Proteins*. Oxford University Press; New York: 1998. p. 279-311.
- Bearne SL, Wolfenden R. Mandelate racemase in pieces: effective concentrations of enzyme functional groups in the transition state. *Biochemistry*. 1997; 36:1646–1656. [PubMed: 9048548]
- St Maurice M, Bearne SL. Kinetics and thermodynamics of mandelate racemase catalysis. *Biochemistry*. 2002; 41:4048–4058. [PubMed: 11900548]
- Babbitt PC, Gerlt JA. Understanding enzyme superfamilies. Chemistry as the fundamental determinant in the evolution of new catalytic activities. *J Biol Chem*. 1997; 272:30591–30594. [PubMed: 9388188]
- Babbitt PC, Hasson MS, Wedekind JE, Palmer DR, Barrett WC, Reed GH, Rayment I, Ringe D, Kenyon GL, Gerlt JA. The enolase superfamily: a general strategy for enzyme-catalyzed abstraction of the alpha-protons of carboxylic acids. *Biochemistry*. 1996; 35:16489–16501. [PubMed: 8987982]
- Gerlt JA, Gassman PG. Understanding the rates of certain enzyme-catalyzed reactions: proton abstraction from carbon acids, acyl-transfer reactions, and displacement reactions of phosphodiester. *Biochemistry*. 1993; 32:11943–11952. [PubMed: 8218268]
- Gerlt JA, Kenyon GL, Kozarich JW, Neidhart DC, Petsko GA. Mandelate racemase and class-related enzymes. *Curr Opin Struct Biol*. 1992; 2:736–742.
- Radzicka A, Wolfenden R. Transition state and multisubstrate analog inhibitors. *Methods Enzymol*. 1995; 249:284–312. [PubMed: 7791615]
- Schramm VL. Enzymatic transition state poise and transition state analogues. *Acc Chem Res*. 2003; 36:588–596. [PubMed: 12924955]
- Schramm VL. Enzymatic transition state theory and transition state analogue design. *J Biol Chem*. 2007; 282:28297–28300. [PubMed: 17690091]
- Schramm VL. Enzymatic transition states and transition state analog design. *Annu Rev Biochem*. 1998; 67:693–720. [PubMed: 9759501]
- Wolfenden, R.; Frick, L. Transition state affinity and the design of enzyme inhibitors. In: Page, ML.; Williams, A., editors. *Enzyme Mechanisms*. Royal Society of Chemistry; London: 1987. p. 97-122.

13. Bourque JR, Burley RK, Bearne SL. Intermediate analogue inhibitors of mandelate racemase: *N*-Hydroxyformanilide and cupferron. *Bioorg Med Chem Lett*. 2007; 17:105–108. [PubMed: 17055725]
14. Burley RK, Bearne SL. Inhibition of mandelate racemase by the substrate-intermediate-product analogue 1,1-diphenyl-1-hydroxymethylphosphonate. *Bioorg Med Chem Lett*. 2005; 15:4342–4344. [PubMed: 16039120]
15. St Maurice M, Bearne SL. Reaction intermediate analogues for mandelate racemase: interaction between Asn 197 and the α -hydroxyl of the substrate promotes catalysis. *Biochemistry*. 2000; 39:13324–13335. [PubMed: 11063568]
16. St Maurice M, Bearne SL, Lu W, Taylor SD. Inhibition of Mandelate Racemase by α -Fluorobenzylphosphonates. *Bioorg Med Chem Lett*. 2003; 13:2041–2044. [PubMed: 12781191]
17. Narmandakh A, Bearne SL. Purification of recombinant mandelate racemase: improved catalytic activity. *Protein Expr Purif*. 2010; 69:39–46. [PubMed: 19589387]
18. St Maurice, M. *Biochemistry & Molecular Biology*. Dalhousie; Halifax: 2003. The role of binding determinants in ground state and transition state stabilization by mandelate racemase; p. 244
19. Siddiqi F, Bourque JR, Jiang H, Gardner M, St Maurice M, Blouin C, Bearne SL. Perturbing the hydrophobic pocket of mandelate racemase to probe phenyl motion during catalysis. *Biochemistry*. 2005; 44 in press.
20. Bourque JR, Bearne SL. Mutational analysis of the active site flap (20s loop) of mandelate racemase. *Biochemistry*. 2008; 47:566–578. [PubMed: 18092808]
21. Sharp TR, Hegeman GD, Kenyon GL. A direct kinetic assay for mandelate racemase using circular dichroic measurements. *Anal Biochem*. 1979; 94:329–334. [PubMed: 464301]
22. Gasteiger E, Gattiker A, Hoogland C, Ivanyi I, Appel RD, Bairoch A. ExPASy: The proteomics server for in-depth protein knowledge and analysis. *Nucleic Acids Res*. 2003; 31:3784–3788. [PubMed: 12824418]
23. Otwinowski Z, Minor W. Processing of X-ray diffraction data collected in oscillation mode. *Methods Enzymol*. 1997; 276:307–326.
24. McCoy AJ, Grosse-Kunstleve RW, Adams PD, Winn MD, Storoni LC, Read RJ. Phaser crystallographic software. *J Appl Cryst*. 2007; 40:658–674. [PubMed: 19461840]
25. Emsley P, Lohkamp B, Scott WG, Cowtan K. Features and development of *Coot*. *Acta Cryst D*. 2010; 66:486–501. [PubMed: 20383002]
26. Vagin AA, Steiner RS, Lebedev AA, Potterton L, McNicholas S, Long F, Murshudov GN. REFMAC5 dictionary: organisation of prior chemical knowledge and guidelines for its use. *Acta Cryst D*. 2004; 60:2284–2295.
27. Moriarty NW, Grosse-Kunstleve RW, Adams PD. Electronic Ligand Builder and Optimization Workbench (eLBOW): a tool for ligand coordinate and restraint generation. *Acta Cryst D*. 2009; 65:1074–1080. [PubMed: 19770504]
28. Gulick AM, Hubbard BK, Gerlt JA, Rayment I. Evolution of enzymatic activities in the enolase superfamily: crystallographic and mutagenesis studies of the reaction catalyzed by D-glucarate dehydratase from *Escherichia coli*. *Biochemistry*. 2000; 39:4590–4602. [PubMed: 10769114]
29. Poyner RR, Reed GH. Structure of the bis divalent cation complex with phosphonoacetohydroxamate at the active site of enolase. *Biochemistry*. 1992; 31:7166–7173. [PubMed: 1322695]
30. Wedekind JE, Poyner RR, Reed GH, Rayment I. Chelation of serine 39 to Mg²⁺ latches a gate at the active site of enolase: structure of the bis(Mg²⁺) complex of yeast enolase and the intermediate analog phosphonoacetohydroxamate at 2.1-Å resolution. *Biochemistry*. 1994; 33:9333–9342. [PubMed: 8049235]
31. Yew WS, Fedorov AA, Fedorov EV, Almo SC, Gerlt JA. Evolution of enzymatic activities in the enolase superfamily: L-talarate/galactarate dehydratase from *Salmonella typhimurium* LT2. *Biochemistry*. 2007; 46:9564–9577. [PubMed: 17649980]
32. Bartlett PA, Marlowe CK. Phosphoramidates as transition-state analogue inhibitors of thermolysin. *Biochemistry*. 1983; 22:4618–4624. [PubMed: 6626519]

33. Phillips MA, Kaplan AP, Rutter WJ, Bartlett PA. Transition-state characterization: a new approach combining inhibitor analogues and variation in enzyme structure. *Biochemistry*. 1992; 31:959–963. [PubMed: 1734971]
34. Exner O, Hradil M, Mollin J. Dissociation of hydroxamic acids: solvent effects. *Collect Czech Chem Commun*. 1993; 58:1109–1121.
35. Farkas E, Enyedy EA, Csoka H. Some factors affecting metal ion-monohydroxamate interactions in aqueous solution. *J Inorg Biochem*. 2000; 79:205–211. [PubMed: 10830867]
36. Pyatnitkii IV. Dissociation constant of nitrosophenylhydroxylamine. *Zh Anal Khim*. 1946; 1:135–139.
37. Lobanov FI, Savostina VM, Peshkova VM. Complexing of titanium(IV) with cupferron in an acid medium. *Khimiya*. 1969; 24:95–97.
38. Martell, AE.; Smith, RM. *Critical Stability Constants*. Vol. 3. Plenum Press; New York: 1977.
39. Gerlt JA, Gassman PG. An explanation for rapid enzyme-catalyzed proton abstraction from carbon acids: importance of late transition states in concerted mechanisms. *J Am Chem Soc*. 1993; 115:11552–11568.
40. Neidhart DJ, Howell PL, Petsko GA, Powers VM, Li RS, Kenyon GL, Gerlt JA. Mechanism of the reaction catalyzed by mandelate racemase. 2 Crystal structure of mandelate racemase at 2.5-Å resolution: identification of the active site and possible catalytic residues. *Biochemistry*. 1991; 30:9264–9273. [PubMed: 1892834]
41. Kallarakal AT, Mitra B, Kozarich JW, Gerlt JA, Clifton JG, Petsko GA, Kenyon GL. Mechanism of the reaction catalyzed by mandelate racemase: structure and mechanistic properties of the K166R mutant. *Biochemistry*. 1995; 34:2788–2797. [PubMed: 7893690]
42. Landro JA, Gerlt JA, Kozarich JW, Koo CW, Shah VJ, Kenyon GL, Neidhart DJ, Fujita S, Petsko GA. The role of lysine 166 in the mechanism of mandelate racemase from *Pseudomonas putida*: mechanistic and crystallographic evidence for stereospecific alkylation by (*R*)- α -phenylglycidate. *Biochemistry*. 1994; 33:635–643. [PubMed: 8292591]
43. Schafer SL, Barrett WC, Kallarakal AT, Mitra B, Kozarich JW, Gerlt JA, Clifton JG, Petsko GA, Kenyon GL. Mechanism of the reaction catalyzed by mandelate racemase: structure and mechanistic properties of the D270N mutant. *Biochemistry*. 1996; 35:5662–5669. [PubMed: 8639525]
44. Mitra B, Gerlt JA, Babbitt PC, Koo CW, Kenyon GL, Joseph D, Petsko GA. A novel structural basis for membrane association of a protein: construction of a chimeric soluble mutant of (*S*)-mandelate dehydrogenase from *Pseudomonas putida*. *Biochemistry*. 1993; 32:12959–12967. [PubMed: 8241149]
45. Whitman CP, Hegeman GD, Cleland WW, Kenyon GL. Symmetry and asymmetry in mandelate racemase catalysis. *Biochemistry*. 1985; 24:3936–3942. [PubMed: 2996586]
46. St Maurice M, Bearne SL. Hydrophobic nature of the active site of mandelate racemase. *Biochemistry*. 2004; 43:2524–2532. [PubMed: 14992589]
47. Kleywegt, GJ.; Zou, JY.; Kjeldgaard, M.; Jones, TA. Around O. In: Rossmann, MG.; Arnold, E., editors. *International Tables for Crystallography, Vol F Crystallography of Biological Macromolecules*. Vol. 353–356. Dordrecht: Kluwer Academic Publishers, The Netherlands; 2001. p. 366–367.
48. Kim SJ, Yoon CJ, Chang IS. Studies on metal cupferrate complexes in mixed solvents. *J Korean Chem Soc*. 1969; 13:16–24.
49. Gerlt JA, Babbitt PC, Rayment I. Divergent evolution in the enolase superfamily: the interplay of mechanism and specificity. *Arch Biochem Biophys*. 2005; 433:59–70. [PubMed: 15581566]
50. Rakus JF, Fedorov AA, Fedorov EV, Glasner ME, Hubbard BK, Delli JD, Babbitt PC, Almo SC, Gerlt JA. Evolution of enzymatic activities in the enolase superfamily: L-rhamnonate dehydratase. *Biochemistry*. 2008; 47:9944–9954. [PubMed: 18754693]
51. Taylor DK, Bytheway I, Barton DHR, Bayse CA, Hall MB. Toward the generation of NO in Biological systems. Theoretical studies of the N₂O₂ Grouping. *J Org Chem*. 1995; 60:435–444.
52. Sjöberg P, Politzer P. Use of the Electrostatic Potential at the Molecular Surface To Interpret and Predict Nucleophilic Processes. *J Phys Chem*. 1990; 94:3959–3961.

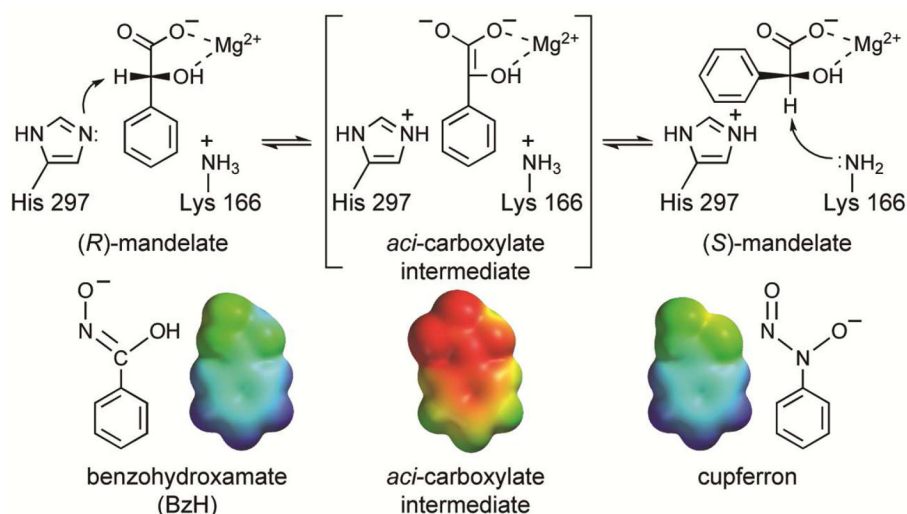


Figure 1.

The two-base mechanism for MR-catalyzed racemization of (*R*)- and (*S*) mandelate is illustrated. The molecular electrostatic potential surface (EPS) at the van der Waals radii for the conjugate base of Z-BzH (*O*-deprotonated (34)), the putative *aci*-carboxylate intermediate, and the conjugate base of Z-cupferron (51) are also shown. EPSs have an electron density isosurface displayed at a density of 0.002 e/a_0^3 which encompasses approximately 95% of the van der Waals radii (52). The energy difference from the red (negative potentials) to blue (more electropositive potentials) regions of the EPSs is 150 kcal/mol with the more electropositive positive potential fixed at an upper limit of -50 kcal/mol for all molecules. Geometry optimizations and ESPs were calculated using the density functional B3LYP/6-311+G** method with *Spartan'04 Windows* v. 1.0.1 (Wavefunction, Inc., Irvine, CA).

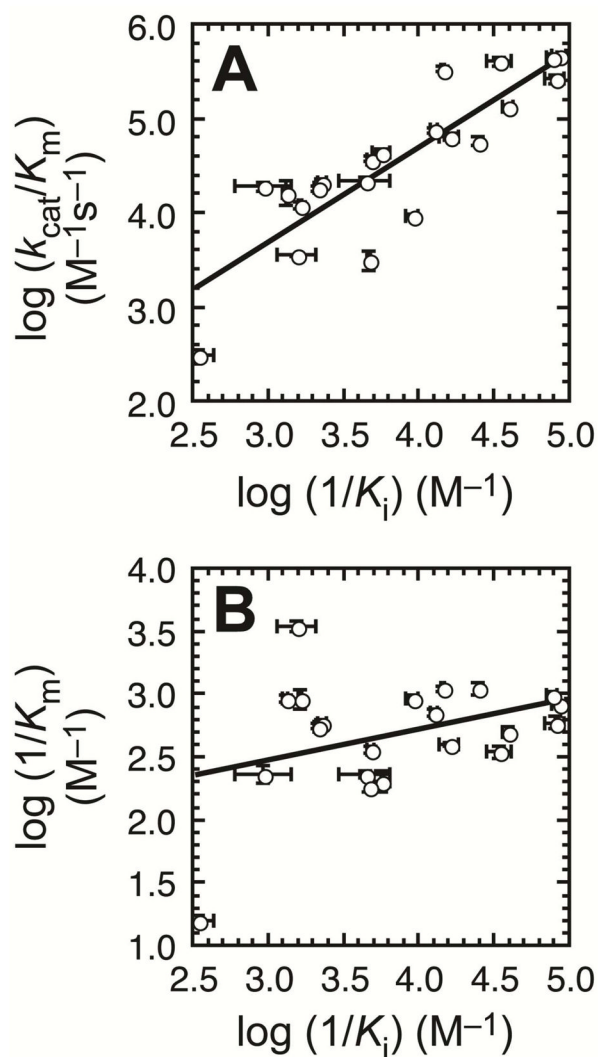


Figure 2.

Linear free energy relationships between K_i values for the competitive inhibition of MR variants by benzohydroxamate and the corresponding k_{cat}/K_m (panel A) and K_m (panel B) values for the variants. The curves shown are the linear regression lines with values for the slope, y-intercept, and correlation coefficient (r^2) equal to 1.01 ± 0.14 , 0.65 ± 0.54 , and 0.7379 for panel A and 0.25 ± 0.14 , 1.72 ± 0.56 , and 0.1406 for panel B.

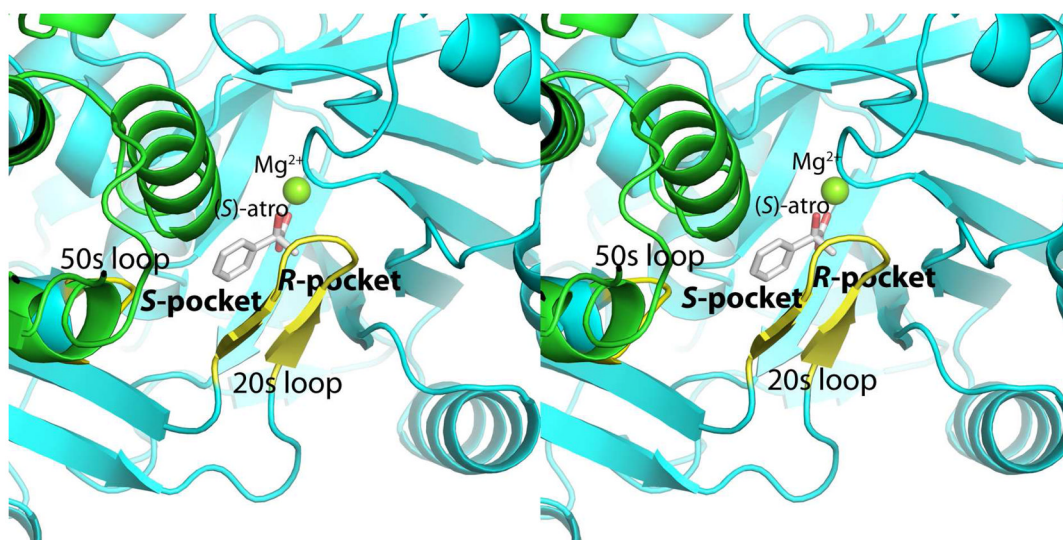


Figure 3.

Stereoview of the representative active site architecture of MR with Mg^{2+} and (*S*)-atrolactate ((*S*)-atro) bound in the enzyme active site (pdb 1MDR). The active site has been proposed to include an *R*-specific and *S*-specific pocket, which bind the phenyl group of (*R*)- and (*S*)-mandelate, respectively (19, 46). The *S*-specific pocket is composed of residues from the 50s loop (colored in yellow) and residues 90–95 of a neighboring subunit (colored in green). The *R*-specific pocket is comprised primarily of residues in the 20s loop (colored in yellow). The phenyl ring must translocate between the *R*- and *S*-specific pockets during catalysis (see Results and Discussion).

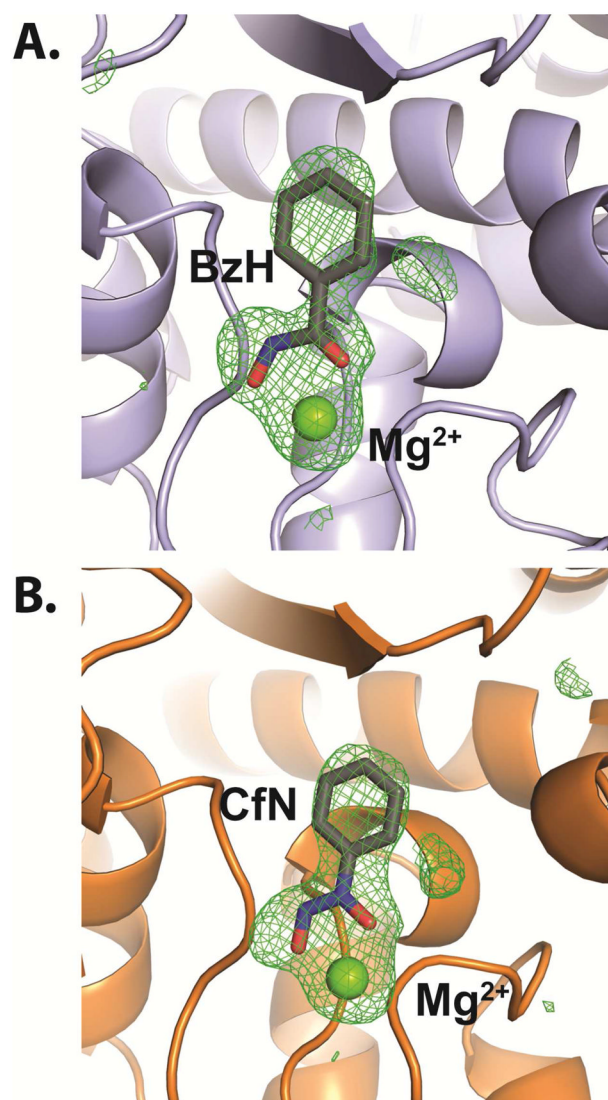
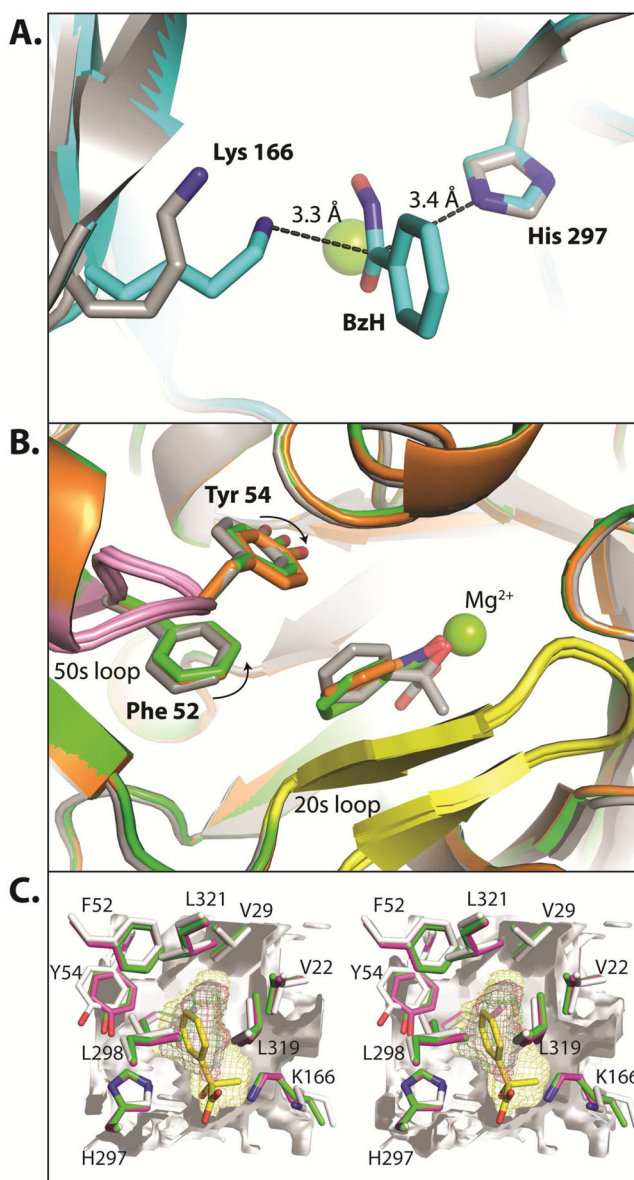


Figure 4. Representative simulated-annealing omit maps for Mg^{2+} -BzH (**A**) and Mg^{2+} -CfN (**B**) in the active site of MR are shown. The electron density maps are contoured at 3.0σ and extend to a distance of 7 \AA from the ligand.

**Figure 5.**

Side chain movements associated with intermediate analogue binding. **(A)** Structural overlay of the MR-BzH complex with the MR-(*S*)-atrolactate complex (pdb 1MDR). The catalytic amino acid side chain positions are colored in grey for the structure in the presence of (*S*)-atrolactate and in blue for the structure in the presence of BzH. The (*S*)-specific general base catalyst, Lys 166, is repositioned in the presence of the planar intermediate analogue such that the ϵ -nitrogen is 3.3 Å from the α -carbon of BzH. This distance is equal to that of the (*R*)-specific general base catalyst, His 297, from the α -carbon of BzH. **(B)** Structural overlay of the MR-BzH complex (green), the MR-CfN complex (orange), and the MR-(*S*)-atrolactate complex (pdb 1MDR, grey). Both Tyr 54 and Phe 52 move into closer proximity with the intermediate analogues, providing structural evidence for a more constrained hydrophobic cavity in the intermediate-bound state. The 20s and 50s loops are colored in yellow and pink, respectively. These loops do not exhibit any significant motion accompanying the binding of the planar intermediate analogues. **(C)** Stereoview illustrating

the variation in active site cavities in the 1MDR (white), BzH (pink), and CfN (green) dimers. The volume reduction in the intermediate analogue structures comes from movement of the Lys 166 side chain along with a slight inward movement of the backbone chain connecting the end of this β -strand to the subsequent α -helix; and from a general constriction of the hydrophobic cavity. Cavity volumes were calculated with a water probe at the van der Waals radius of 1.4 Å using the program VOIDOO (47). All calculations were performed on a single active site with the ligand and Mg^{2+} removed and the contribution to the active site from the dimerization interface included. In all cases, the cavity search was initiated at the equivalent of the β -carbon position of (*S*)-atrolactate in chain A, after all pdb files had been structurally overlaid for chain A. The calculated protein surface lining the 1MDR cavity (over a $14 \times 14 \times 12$ Å grid map) is displayed as a partially translucent white isosurface. The yellow mesh illustrates the active site cavity in 1MDR, the green mesh for MR-CfN, and the pink mesh for MR-BzH. (*S*)- Atrolactate is illustrated as yellow sticks. All residues lining the cavity are shown and labeled. Leu 93' from the neighboring chain can be seen behind (*S*)-atrolactate and, for clarity, is not labeled.

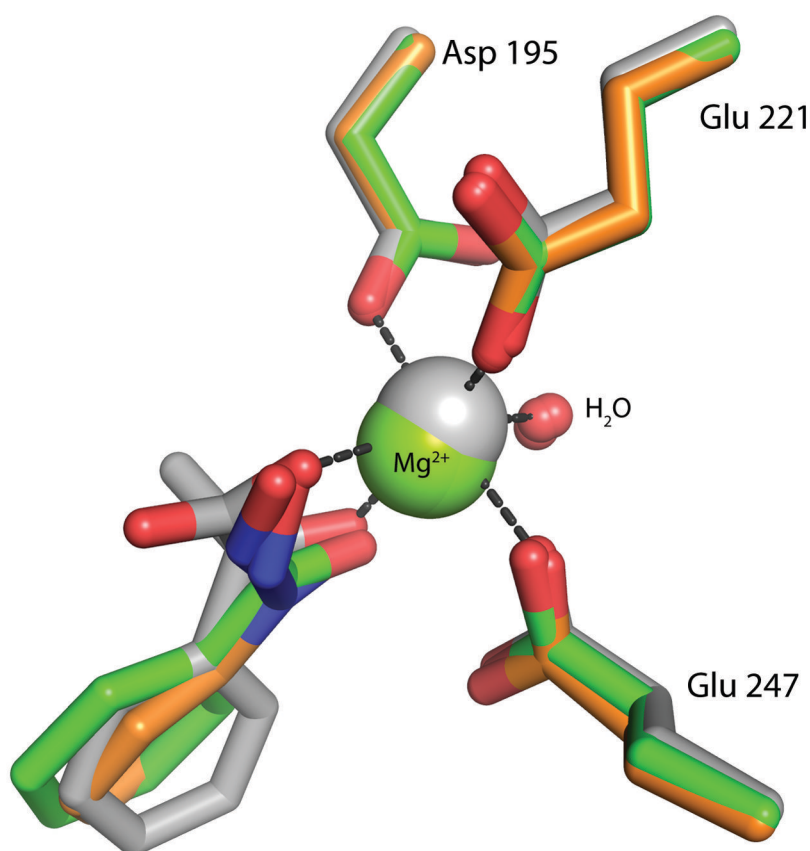


Figure 6.

Structural overlay of the Mg²⁺-binding residues in the MR-BzH complex (green), the MR-CfN complex (orange), and the MR-(*S*)-atrolactate complex (pdb 1MDR, grey). The positions of all atoms coordinating the Mg²⁺ are nearly identical in all three structures. The Mg²⁺ ion is bound in closer proximity to CfN and BzH than it is to (*S*)-atrolactate, consistent with the enhanced Mg²⁺-binding affinity expected for these analogues (35, 48).

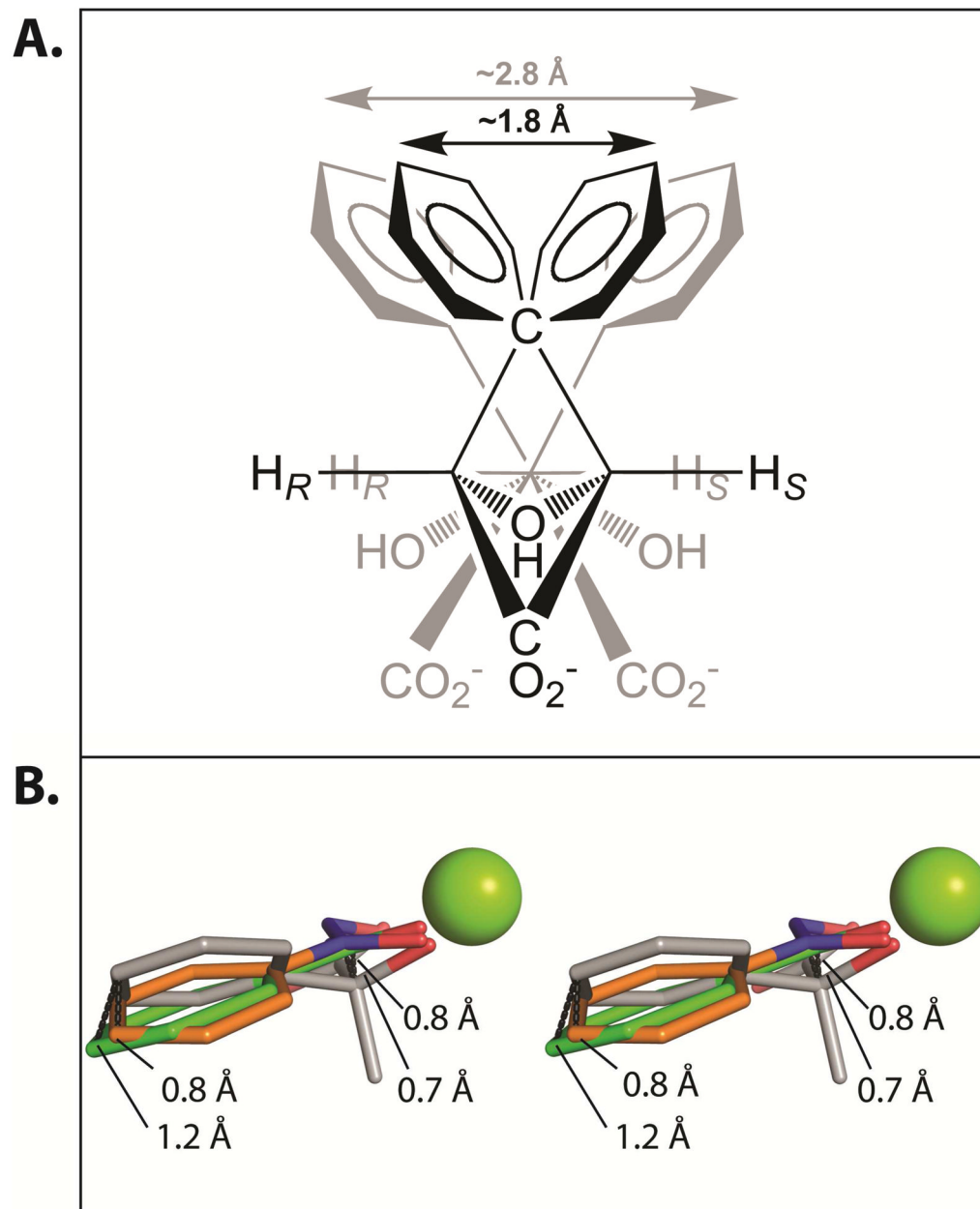


Figure 7.

Motion of the phenyl group during catalysis. **(A)** Schematic diagram depicting two scenarios which illustrate the magnitude of motion that the phenyl ring of mandelate may undergo during catalysis. Superimposed structures of (*R*)- and (*S*)-mandelate are shown bound at the active site of MR. If the position of the α -carbon remains fixed as the substrate undergoes a Walden inversion (grey structures), then the *para*-carbon atom of the phenyl ring may traverse ~ 2.8 Å during catalysis. However, if the α -carbon atom moves (~ 1.0 Å) so that the hydroxyl, carboxylate, and β -carbon remain bound in the same plane as the substrate undergoes a Walden inversion (black structures), the *para*-carbon atom of the phenyl ring may traverse ~ 1.8 Å during catalysis. **(B)** Stereoview of the ligands from superpositioned structures of MR complexed with (*S*)-atrolactate (pdb 1MDR, grey), BzH (green) and CfN

(orange). From these structures, the *para*-carbon of the phenyl group moves 0.8–1.2 Å, the α -carbon moves 0.7–0.8 Å and the β -carbon remains fixed.

Table 1

Data Collection and Refinement Statistics

	MR + BzH	MR + CfN
PDB ID code	3UXK	3UXL
Space Group	I 4	I 4
Cell Dimensions		
<i>a</i> , <i>b</i> , <i>c</i> (Å)	148, 148, 170	148, 148, 175
α , β , γ (°)	90, 90, 90	90, 90, 90
Resolution range, Å	50.0–2.20 (2.24–2.20) ^a	50.0–2.20 (2.24–2.20) ^a
Redundancy	7.6 (7.1)	4.2 (3.8)
Completeness (%)	100 (100)	100 (100)
Unique Reflections	92 311	95 130
R _{merge} (%)	10.5 (25.3)	8.5 (31.7)
Average I/σ	28.0 (8.3)	17.5 (3.6)
Refinement:		
Resolution range, Å	50.0–2.20 (2.26–2.20)	50.0–2.20 (2.26–2.20)
R _{cryst}	0.162 (0.171)	0.182 (0.205)
R _{free}	0.193 (0.204)	0.227 (0.249)
No. protein atoms	11 529	11 280
No. water molecules	749	565
Wilson B-value (Å ²)	27.7	32.8
Average B-factors (Å ²)		
Protein	17.2	24.5
Ligands	40.7	37.9
Mg ²⁺	12.7	15.4
Solvent	21.0	25.3
Ramachandran (%)		
Most favored	90.6	90.6
Additionally allowed	8.7	8.7
Generously allowed	0.3	0.3
Disallowed	0.3	0.3
r.m.s. deviations		
Bond lengths (Å)	0.014	0.015
Bond angles (°)	1.355	1.641

^aValues in parentheses are for the highest resolution bin.

Table 2

Kinetic constants (K_{cat} , K_{m} , and $K_{\text{cat}}/K_{\text{m}}$) and competitive inhibition constants (K_{i}) for the inhibition of MR variants by benzohydroxamate^a

MR	Kinetic constants ($R \rightarrow S$)			K_{i}
variant	K_{m} (mM)	k_{cat} (s ⁻¹)	$k_{\text{cat}}/K_{\text{m}}$ (M ⁻¹ s ⁻¹)	μM
wild-type ^b	1.20 ± 0.04 (0.97 ± 0.09) ^c	552 ± 6 (470 ± 10) ^c	4.6 (± 0.2) × 10 ⁵ (4.8 (± 0.3) × 10 ⁵) ^c	11.7 ± 1.2
Y54F	1.02 ± 0.06 (0.90 ± 0.08) ^c	456 ± 16 (397 ± 21) ^c	4.5 (± 0.3) × 10 ⁵ (4.4 (± 0.5) × 10 ⁵) ^c	13.1 ± 1.1
Y54L	2.0 ± 0.2 (2.3 ± 0.3) ^c	253 ± 4 (301 ± 9) ^c	1.3 (± 0.1) × 10 ⁵ (1.3 (± 0.2) × 10 ⁵) ^c	25.7 ± 1.9
V22A ^b	4.4 ± 0.7	82 ± 3	1.9 (± 0.2) × 10 ⁴	1080 ± 460
V22I ^{b, d}	2.9 ± 0.3	1.15 (± 0.05) × 10 ³	4.0 (± 0.4) × 10 ⁵	29.2 ± 5.2
V22F ^b	4.4 ± 0.3	98 ± 3	2.2 (± 0.2) × 10 ⁴	229.0 ± 86.6
T24S ^b	2.8 ± 0.2	102 ± 2	3.7 (± 0.2) × 10 ⁴	209.5 ± 9.9
A25V ^b	1.1 ± 0.2	13 ± 1	1.2 (± 0.1) × 10 ⁴	610.6 ± 12.2
V26A ^b	0.91 ± 0.05	304 ± 3	3.3 (± 0.2) × 10 ⁵	69.3 ± 2.2
V26L ^b	1.7 ± 0.1	36 ± 4	2.1 (± 0.2) × 10 ⁴	440.4 ± 26.9
V26F ^b	1.8 ± 0.1	33 ± 1	1.8 (± 0.1) × 10 ⁴	461.6 ± 31.7
V26A/V29L ^b	1.4 ± 0.1	106 ± 0.4	7.5 (± 0.5) × 10 ⁴	79.2 ± 3.6
V29A ^b	5 ± 1	2.4 (± 0.2) × 10 ²	4.4 (± 0.4) × 10 ⁴	178.6 ± 23.3
V29L ^b	1.7 ± 0.2	3.0 (± 0.1) × 10 ²	2.6 (± 0.3) × 10 ⁵	12.5 ± 1.8
V29F ^b	0.9 ± 0.1	53 ± 1	5.7 (± 0.7) × 10 ⁴	40.1 ± 0.2
V29D ^e	63 ± 6	19 ± 2	3.1 (± 0.4) × 10 ²	2900 ± 700
N197A ^f	5.40 ± 0.66	16.9 ± 3.5	3.1 (± 0.7) × 10 ³	216 ± 6
E317Q ^e	1.10 ± 0.07	0.18 ± 0.05	1.6 (± 0.5) × 10 ⁴	760 ± 31
F52W ^g	2.5 ± 0.1	159 ± 17	6.4 (± 0.5) × 10 ⁴	63 ± 10
Y54W ^{g, h}	1.1 ± 0.1	10 ± 1	9.3 (± 0.4) × 10 ³	110 ± 10
F52W/Y54W ^g	0.29 ± 0.03	1.0 ± 0.1	3.5 (± 0.1) × 10 ³	640 ± 190

^aValues are means of triplicate trials and reported errors are the standard deviations.

^bKinetic constants k_{cat} , K_{m} , and $k_{\text{cat}}/K_{\text{m}}$ are from reference (20).

^cKinetic parameters in the $S \rightarrow R$ reaction direction.

^dKinetic parameters determined using 20 mM Mg²⁺.

^eValues of k_{cat} , K_{m} , $k_{\text{cat}}/K_{\text{m}}$, and K_{i} are from reference (18).

^fValues of k_{cat} , K_{m} , $k_{\text{cat}}/K_{\text{m}}$, and K_{i} are from reference (15).

^gValues of k_{cat} , K_{m} , $k_{\text{cat}}/K_{\text{m}}$, and K_{i} are from reference (19).

^hKinetic constants determined using 15 mM Mg²⁺.